

## MODELING AND INTERPRETATION OF STM IMAGES OF CARBON NANOSYSTEMS

G. I. MÁRK<sup>1,2</sup>, L. P. BIRÓ<sup>2</sup>, AND PH. LAMBIN<sup>1</sup>

<sup>1</sup>*Département de Physique, Facultés Universitaires N.D.P.  
61 Rue de Bruxelles, B 5000 Namur, Belgium*

<sup>2</sup>*Research Institute for Technical Physics and Materials Science  
H-1525 Budapest P.O.Box 49, Hungary  
EMail: mark@sunserv.kfki.hu*

**Abstract.** Scanning tunneling microscopy (STM) is the only tool making it possible to study both the topography and electronic structure of carbon nanosystems in sub-nanometer resolution. The interpretation of the STM images of carbon nanosystems is more complicated than in the case of flat, single crystalline surfaces. Because of this computer simulation is a helpful tool in understanding the experimental data. In this paper the image formation in STM and the particularities of imaging supported carbon nanosystems are discussed. The tight binding and the wave packet dynamical STM simulation methods are reviewed with applications showing their complementary merits. These methods are simple enough to make feasible in the near future their application to more complex carbon nanosystems like coiled nanotubes and nanotube crossings.

### 1. Introduction

The discovery of the fullerene [1] opened a new era of carbon science: the science of carbon nanostructures. For the time being a large variety of these systems [2] are known: fullerenes [1,3], carbon nanotubes [3,4], peapods [5], nanotube junctions [6], Y-connections [7], aggregations of nanotubes, carbon onions, etc. Apart from being very interesting from the theoretical point of view, carbon nanostructures have a wide range of potential applications owing to their remarkable mechanical and electrical properties. There are not many tools available to characterize isolated carbon nanostructures. Among these techniques only scanning tunneling microscopy (STM) gives

the possibility to study both the topography and the electronic structure of these nanosystems in sub-nanometer resolution. However, this very property of STM makes it not easy to interpret STM images because the influence of the topography and the electronic structure has to be separated. Several other factors, from which the STM tip geometry is the most important, also influence the imaging mechanism. Because of all these features image simulation is inevitable for a correct interpretation of STM images.

## 2. Scanning Tunneling Microscopy

In the STM instrument [8] an atomically sharp, conducting tip is brought within a distance of a few tenths of a nanometer to a conducting surface (sample) while an  $U_t$  bias of the order of 1 V is applied between the tip and the sample. Because of the small separation a quantum mechanical tunnel current  $I_t$  of the order of 1 nA is flowing through the tip-sample gap. In the most common, so called topographic mode of the STM the tip is mechanically scanned above the sample (in the X-Y plane) by piezo actuators while a feedback loop controls the height of the tip above the sample (Z coordinate of the tip) to maintain the tunnel current at a preselected constant  $I_{setpoint}$  value. The so generated 3D motion of the tip defines the topographic STM image. In practical STM instruments the  $Z(X, Y)$  topographic image is constructed from the  $U_X, U_Y, U_Z$  voltages applied to the piezos.

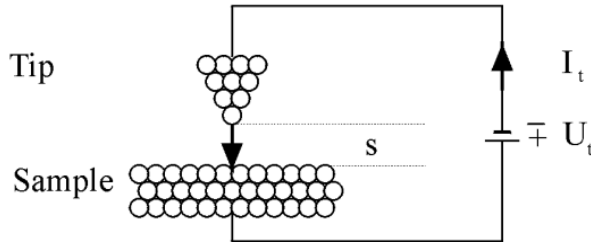


*Figure 1.* Concept of the STM. Small circles symbolize the atoms.  $s$  is the tip-sample tunnel gap.

The simplest explanation of STM operation is based on 1D tunneling theory [9]. When a quantum mechanical particle of energy  $E$  is incident on a potential barrier of height  $V_0$  and width  $s$  the transmission probability is

$$T \propto e^{-2\kappa s}, \quad (1)$$

where

$$\kappa = \sqrt{2m/\hbar^2(V_0 - E)}. \quad (2)$$

This expression is valid in the asymptotic limit of  $\kappa s \gg 1$  (i.e. small transmission).

In an STM instrument, however, one of the electrodes is not a plane, but a sharp tip (see Fig. 1). Because of the exponential dependence of the tunneling probability with distance the majority of the tunnel current flows in a narrow channel between the tip apex and the sample plane. The typical minimum achievable half width at half maximum  $HW_T$  of the tunneling channel is  $0.1 - 0.2 \text{ nm}$  with sharp tips [10]. This narrow tunneling channel is responsible for the atomic resolution of the STM.

## 2.1. STM ON CARBON NANOSTRUCTURES

Carbon nanostructures are 3D objects with characteristic radii of curvature in the  $\text{nm}$  range. This value is comparable on the one hand to the characteristic value of the tip-sample tunnel gap (which is of the order of  $0.5 \text{ nm}$  in typical STM experiments) and on the other hand to the apex radius of the STM tip. This makes the interpretation of STM images of carbon nanostructures different from that of flat surfaces.

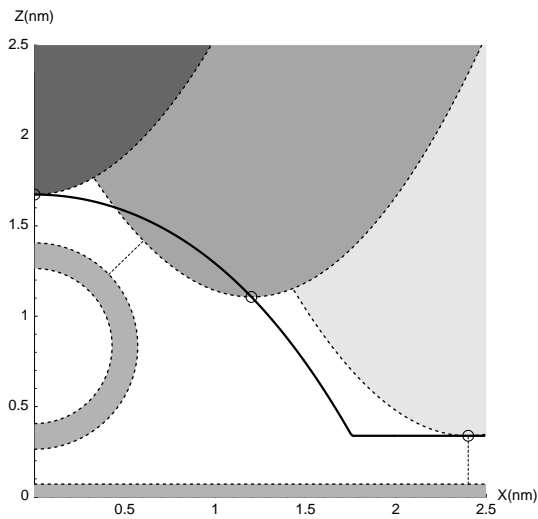


*Figure 2.* Geometric line cut. The thick line is the geometric line cut drawn by the apex of the tip (marked by open circle). The shaded lower half plane, middle ring and upper hyperbolas show the vertical cross sections of the sample, nanotube, and tip, respectively. The electrodes are bounded by their jellium effective surfaces (broken lines). Several, typical tip positions are shown, with different shades of grey. For each tip position shown, the nearest tip and sample points are joined by a thin dashed line.

The effect of the comparable characteristic radii of the sample and the tip is generally called “tip convolution effect”. The tip convolution causes a broadening of the sample features as demonstrated on Fig. 2. for the case of a nanotube scanned by a hyperbolic tip. Because of its exponential distance dependence the tunneling current tends to follow the shortest path, which is normal to the tube, and the corresponding “off- $z$ ” component of the current increases as the tip moves aside to the tube [11]. These shortest path segments are shown on Fig. 2. by dashed lines. During the lateral scanning  $I_t$  is kept constant by the feedback loop. Assuming a uniform local density of states (LDOS) on the sample and tip surfaces the effect of the feedback loop can be taken into account approximately by keeping the length of the tunneling path at a constant value. The curve drawn by the apex point of the tip when using this simple approximation is called a *geometric line cut*. As it is demonstrated in Fig. 2., when the tip follows the curvature of the nanotube, the tunneling point moves away gradually from the tip apex to its side. However, when the tip apex approaches the support surface the tunneling is switched back from the side of the tip to the apex. As demonstrated in Sec. 5.3. this simple geometric model is justified by wave packet dynamical calculations.

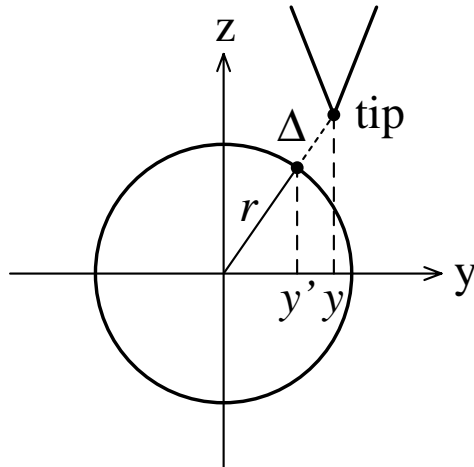


*Figure 3.* Relation between the position of the STM tip ( $y$ ) and that of an imaged atom ( $y'$ ) of the nanotube when the tunneling current follows the shortest path between tip and nanotube (dashed line).

The effect of the comparable values of the characteristic radius of the sample and the tunnel gap is demonstrated in Fig. 3. It causes a stretching

of the image of the atomic lattice in the direction parallel to the sample curvature. To study this effect the tip radius was assumed to be zero throughout the subsequent discussion. Using the geometric approximation discussed above we assume the tip-sample gap to be a constant  $\Delta$  value. (The effect of the atomic lattice causes only a small variation on the order of  $0.1 \text{ nm}$  to this constant gap.) Hence when the tip scans above a nano object with radius of curvature  $r$  its apex moves on a circle of radius  $r + \Delta$ . As a consequence the features on surface of the radius  $r$  are projected onto the radius  $r + \Delta$  surface and are therefore stretched by a factor of  $(r + \Delta)/r$ . In the special case of a carbon nanotube, the radius of curvature is small only in the direction perpendicular to the tube axis (say,  $y$  direction) but it is infinite in the direction parallel to the tube axis ( $x$  direction). This causes an asymmetric stretching in the atomic resolution STM images of small diameter nanotubes: the atomic lattice is inflated in the  $y$  direction. As demonstrated in Sec. 5.3. this stretching is reproduced in tight-binding calculated atomic resolution STM images of carbon nanotubes. It is also seen in experimental STM images taken on single wall nanotubes [12, 13]. Due to the asymmetric distortion, the angles between the C-C nearest neighbor bonds measured on the STM image deviate from  $\pi/3$ .

Apart from the phenomena discussed above, there are other factors specific to the imaging of carbon nanosystems but here we can only give references to these phenomena. These factors include the effect of the different electronic structures of the nanosystem and its support [14], the effect of lattice imperfections and substituted atoms [15], the second tunneling gap [16] (between the nanosystem and the support), point contact effects [17], the lateral spreading of the charge along a nanotube while tunneling [18], etc. All these effects make the simulation of the imaging mechanism an important tool in interpreting STM images and scanning tunneling spectroscopy (STS) curves of carbon nanosystems.

### 3. STM theory

#### 3.1. PERTURBATIC TREATMENT

Treating the tip-sample coupling as a first-order perturbation the total tip-sample current is given as

$$I_t = \frac{2\pi e}{\hbar} \int_{-\infty}^{+\infty} dE [f_t(E) - f_s(E)] \sum_{\alpha, \beta} |\langle \alpha | v | \beta \rangle|^2 \delta(E - E_\alpha) \delta(E - E_\beta) . \quad (3)$$

where  $f_t(E)$  and  $f_s(E)$  are the occupation numbers of the tip and sample, respectively and  $\langle \alpha | v | \beta \rangle$  is the coupling matrix element of an  $|\alpha\rangle$  tip

state to a  $|\beta\rangle$  sample state. This equation is the well-known starting expression of the perturbative theories of elastic tunnel processes.

### 3.2. TERSOFF-HAMANN THEORY

In this simplified model [19] only one atom at the tip apex is taken into account, with an s-wave orbital. Both the tunneling matrix elements and the tip density of states (DOS) are taken to be constant in the  $eU_t$  energy window. With these assumptions the tunnel current is directly proportional to the LDOS integrated between the Fermi level of the tip and sample, that is

$$I_t(\vec{r}, U_t) \propto \int_{E_F^s - eU_t}^{E_F^s} dE \rho_{LDOS}(\vec{r}, E), \quad (4)$$

with

$$\rho_{LDOS}(\vec{r}, E) = \sum_{\beta} |\psi_{\beta}(\vec{r})|^2 \delta(E_{\beta} - E), \quad (5)$$

where  $\psi_{\beta}$  and  $E_{\beta}$  are the electron wavefunction and eigenvalue of state  $\beta$ , respectively. We then approximate the constant current images as iso-surfaces of  $I_t(\vec{r}, U_t)$ . Using this approximation Rubio et al. simulated [20] STM images of single wall nanotubes by determining the  $\rho_{LDOS}(\vec{r}, E)$  values from *ab-initio* calculations.

For an infinitesimally small bias Eq. 4. becomes even simpler:

$$I_t(\vec{r}, U_t) \propto \rho_{LDOS}(\vec{r}, E_F^s), \quad (6)$$

which means that the tunnel current at tip position  $\vec{r}$  is simply proportional to the sample LDOS on the Fermi level at the center of the tip.

### 3.3. TIGHT-BINDING STM THEORY

To go beyond the simple Tersoff-Hamann result one has to make some justified assumptions for the  $\langle \alpha | v | \beta \rangle$  tunneling matrix elements and for the tip DOS. A simplest formalism to accomplish this is the *tight-binding* theory. Assuming just one orbital per atom, the tight-binding expression of the tunnel current takes the following form [21]

$$I_t(U_t) = (2\pi)^2 \frac{e}{h} \int_{E_F^s - eU_t}^{E_F^s} dE \sum_{i, i' \in t} \sum_{j, j' \in s} v_{ij} v_{i'j'}^* n_{ii'}^t (E_F^t - E_F^s + eU_t + E) n_{jj'}^s(E) \quad (7)$$

where the  $E_F$ 's are the Fermi levels of the tip (t) and sample (s),  $v_{ij}$  is a tight-binding coupling between the orbitals located on sites  $i$  of the tip and  $j$  of the sample, and  $n_{jj'}^s(E) = (-1/\pi) \text{Im} G_{jj'}^s(E)$  with  $G_{jj'}^s$  a Green's

function element of the sample. A similar notation,  $n_{I'}^t(E)$ , is defined on the tip side.

For the applications illustrated below, the tip was treated as a single s-atom ( $i$ ), like in Tersoff-Hamann theory, with a Gaussian DOS. On the nanotube, there is one  $\pi$  orbital per C atom ( $j$ ). The tip-sample coupling terms were Slater-Koster sp hopping interactions decaying exponentially with the distance  $d_{ij}$ :

$$v_{ij} = v_0 w_{ij} e^{-d_{ij}/\lambda} \cos \theta_{ij} \quad (8)$$

where  $\theta_{ij}$  is the angle between the  $\pi$  orbital on site  $j$  and the  $ij$  direction, and  $w_{ij}$  is a cutting weight factor

$$w_{ij} = e^{-ad_{ij}^2} / \sum_{j'} e^{-ad_{ij'}^2} \quad (9)$$

introduced for convergence reasons. The parameters are  $\lambda = 0.85 \text{ \AA}$ ,  $a = 0.6 \text{ \AA}^{-2}$ .

#### 4. Wave packet dynamical simulation of the STM image

For a correct interpretation of some effects mentioned in Sec. 2.1. it is necessary to go beyond the first-order perturbation theory. This is the case, e.g. for *point contact imaging* [17] when, because of the small tip-sample separation, the conduction mechanism switches from tunneling to ballistic flow. Point contact imaging is accomplished experimentally by applying relatively large (more than  $1 \text{ nA}$ ) tunnel currents with moderate (less than  $1 \text{ V}$ ) biases. This is because to maintain the small  $R_{tunnel} = U_t/I_t$  value the feedback loop have to push the tip so close to the sample that the potential barrier gets punctured. Atomic resolution is still possible [22] in point contact mode and the switching from tunneling to point contact causes characteristic changes [17] in STS spectra.

In the wave packet dynamical method the current density is determined by calculating the scattering of wave packets (WPs) incident on the barrier potential. The initial WPs are constructed from the stationary states of the reservoir (tip or support bulk) from which the WPs are arriving. The total tunnel current at a given STM bias is calculated as a statistical average of the tunnel currents for WPs of different allowed incident energies and directions ( $\vec{k}$  vectors) weighted according to the band structure of the two reservoirs.

The tunneling probability for a given initial WP is determined from the time dependent wave function  $\psi(\vec{r}, t)$  computed from the time dependent Schrödinger equation by the *split operator Fourier transform method* [14].

In this method the time evolution operator  $\exp(-i\mathbf{H}\Delta t)$  is approximated (in Hartree atomic units) by the symmetrical unitary product

$$\exp(-i\mathbf{H}\Delta t) = \exp(-i\mathbf{K}/2\Delta t) \exp(-i\mathbf{V}\Delta t) \exp(-i\mathbf{K}/2\Delta t) \quad (10)$$

where  $\Delta t$  is the simulation time step. While the effect of the potential energy propagator  $\exp(-i\mathbf{V}\Delta t)$  is a simple multiplication with  $\exp(-iV(\vec{r})\Delta t)$  for local potentials, the kinetic energy propagator  $\exp(-i\mathbf{K}/2\Delta t)$  is applied in  $k$  space by multiplying the  $\varphi(\vec{k}, t)$  momentum space wave function by  $\exp(i|\vec{k}|^2/4\Delta t)$ . To utilise this formula it is necessary to calculate the  $\varphi(\vec{k}, t)$  momentum space wave function by fast Fourier transform (FFT) of  $\psi(\vec{r}, t)$ . Finally we have to return back to real space by inverse FFT.

## 5. Simulation results

### 5.1. GRAPHENE SHEET

As a first application of the tight-binding formalism STM image of a single sheet of graphite (graphene sheet) was calculated, see Fig. 4

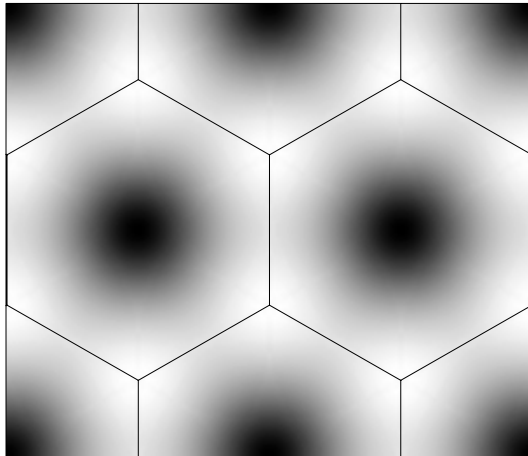


*Figure 4.* STM current map at constant height (0.5 nm) above a graphene sheet. The tip potential is 0.25 V. See the text for details.

We can see corrugation valleys that correspond to the center of the hexagons of the honeycomb structure (overlaid on the image by black lines). Around the hexagonal holes, there is a network of protruding C-C bonds. The hexagonal atomic lattice does not show up in the image, instead a triangular lattice made of the valleys is seen.

## 5.2. BERNAL GRAPHITE

When coupling two or more graphene layers with the Bernal graphite stacking, the two atoms per unit cell become unequivalent: atom A has a neighbor directly beneath whereas atom B does not. In a small interval around the Fermi level, the LDOS on site A is much smaller than that on B [23]. As a result, the STM current at small bias is larger when the tip is above an atom B, which therefore appears as a protrusion in the constant-current image. This interpretation is considered as the ad-hoc explanation of the fact that only every other two atoms are seen in the experimental STM images of graphite [24].

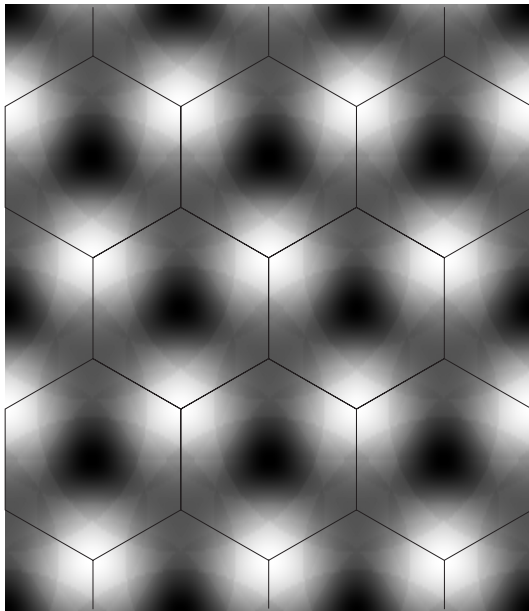


*Figure 5.* STM current map at constant height (0.5 nm) above a multilayer graphite surface. The tip potential is 0.25 V, which corresponds to a current ratio  $I_B/I_A = 2$ . The B atoms are clearly resolved, whereas the A atoms do not come out. See the text for details.

As can be seen in Fig. 5. there are no marked local maxima of the current at the locations of the A atoms, only the B atoms are seen (as white features). By increasing the bias, the differences between the densities of states on A and B sites become less important and the asymmetry washes out gradually.

## 5.3. SINGLE WALL NANOTUBES

Fig. 6. shows the STM images computed by the tight-binding formalism for four single-wall nanotubes with diameter around 1.4 nm.

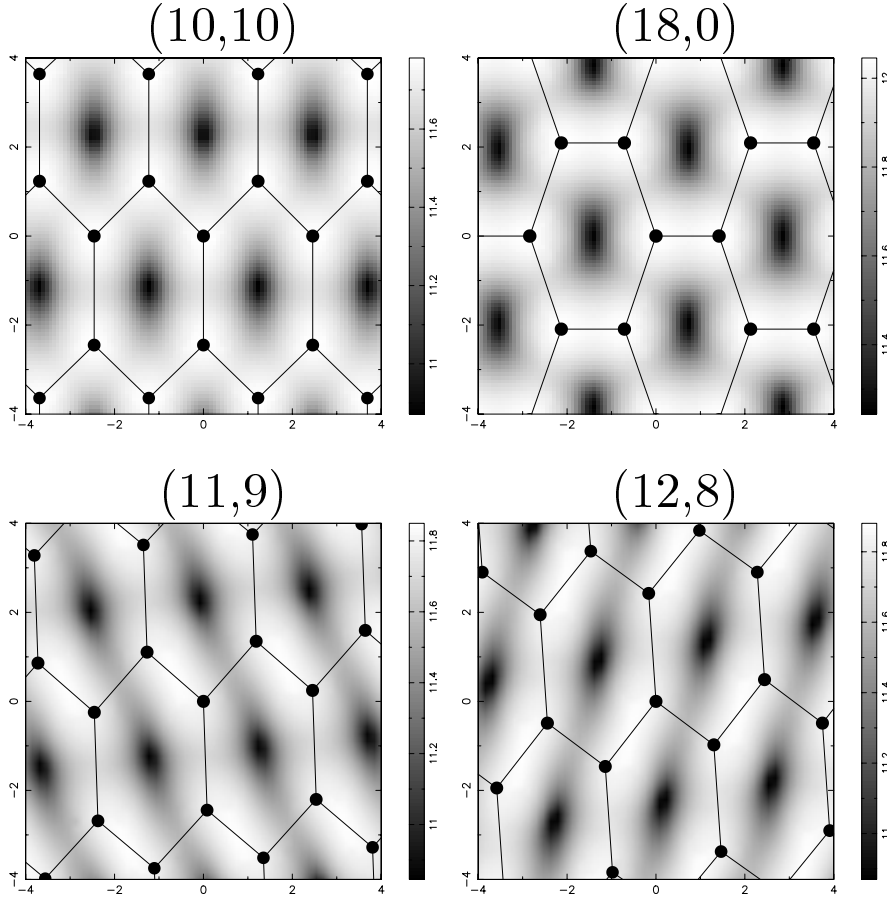


*Figure 6.* Gray-scale representation of the axial distance at constant current of the STM tip apex above the topmost part of four single-wall carbon nanotubes. The tube axis is parallel to the horizontal direction. The vertical distance of the tip to the atom located at the center of each image was set to 0.5 nm. For the two metallic, non-chiral (10,10) and (18,0) nanotubes, the tip potential was 0.3 V. The chiral (11,9) and (12,8) nanotubes are semiconductors, with a band gap of  $\sim 0.6$  eV. For both of them, the tip potential was 0.5 V. All coordinates in the figure are in  $\text{\AA}$ .

In agreement with the interpretation of graphene images summarized above, the centers of the honeycomb hexagons correspond to sharp dips of corrugation. In these two-dimensional maps of the radial distance of the tip, the nanotube axis is along the horizontal,  $x$  direction. Only the

topmost parts of the nanotubes have been imaged. The curvature of the nanotube causes a distortion of the images in the form of an inflation of the  $y$  (see Sec. 2.1.) as discussed in [21], here by a factor of 1.7. This distortion is clearly visible on the honeycomb lattice that was superimposed on the images. It is also responsible for the elongate shape of the corrugation deeps at the center of the hexagons.

In the (18,0) zig-zag nanotube illustrated in Fig. 6, the largest protrusions are found on the bonds parallel to the axis. These protruding bonds form a triangular lattice of oblate humps. This resembles the triangular lattice formed by every other two atoms in multilayered graphite. In the (10,10) armchair nanotube, the largest protrusions are realized on the atoms. Here all the bonds look the same and the image has the honeycomb symmetry. In the case of chiral (11,9) and (12,8) nanotubes, one third of the bonds protrudes more than the others, like with the zig-zag geometry, but not always the ones closest to the axial direction. This bond anisotropy again destroys the hexagonal symmetry, as often observed experimentally [25]. In the chiral nanotubes, the protruding bonds form stripes that spiral around the nanotube [26]. The elongate holes at the center of the hexagons are no longer aligned with the circumference, as indeed often observed in the experimental images [27–29].

Fig. 7. shows snapshots of the time dependent WP probability density for a Gaussian WP incident from the tip bulk onto the tip-nanotube-support tunnel junction. In this calculation focussing on geometrical effects the tunnel junction is modeled by a simple 2D jellium potential [14]. The geometrical and material parameters of the carbon nanotube and the tip are the same as in [14]. The carbon nanotube is modeled by a cylinder of  $0.5 \text{ nm}$  radius floating above the support at a distance of  $0.335 \text{ nm}$ . The STM tip is taken as a hyperbolic cylinder of  $0.5 \text{ nm}$  apex radius and  $15^\circ$  aperture angle. The effective surface of these objects is assumed to be  $0.071 \text{ nm}$  outside their geometric surface (defined as a smooth surface matching the nuclear skeleton of the surface atoms). An infinitesimally small bias is used and all the electrodes are assumed to have the same, free electron metallic DOS. The STM constant current loop is simulated by finding for each  $X_{apex}$  lateral tip displacement that  $Z_{apex}$  vertical tip displacement which yields a constant WP tunneling probability.

With the help of this WP dynamical calculation we are in position to verify the heuristic assumptions made in the derivation of the geometric line cut in Sec. 2.1. It can be seen in Fig. 7. that the majority of the tunnel current is indeed flowing in a narrow channel around the line section connecting the closest points of the tip and the sample, as was sketched intuitively in Fig. 2. For  $X_{apex} = 1.6 \text{ nm}$  we can observe the switching of the tunneling point from the side to the apex of the tip.

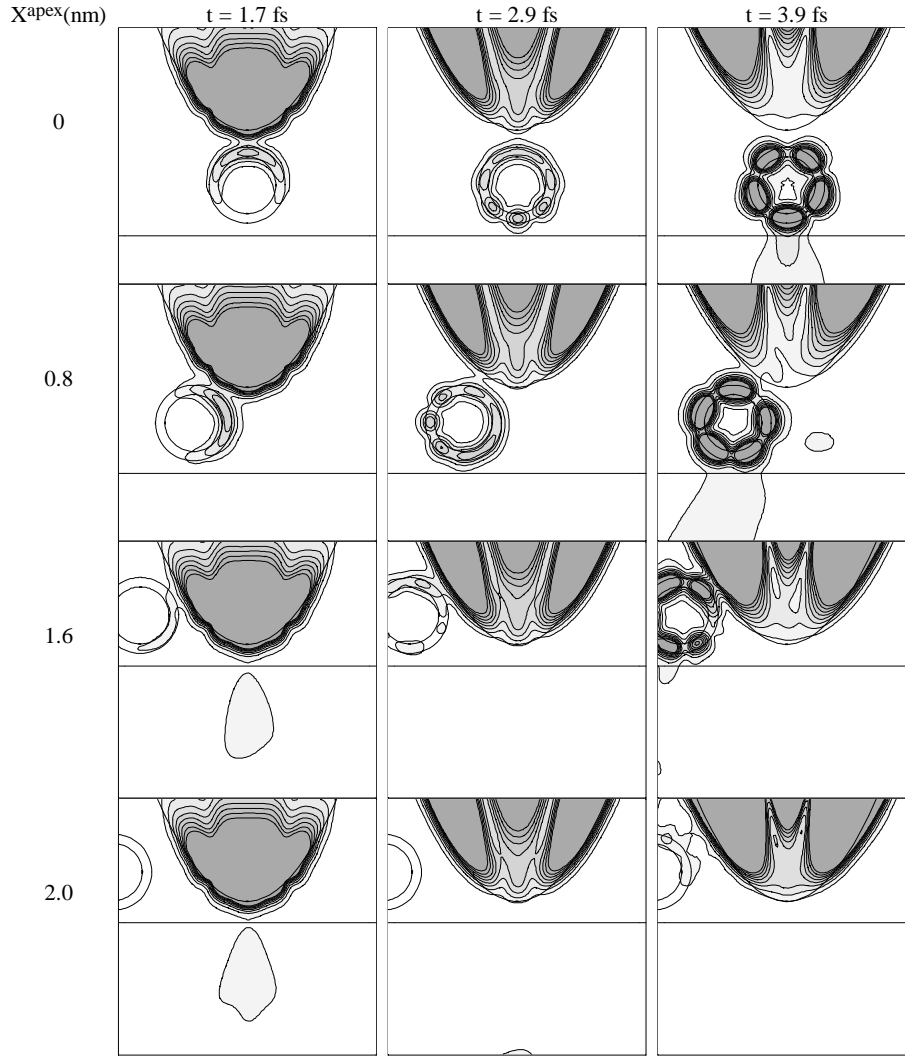


*Figure 7.* Probability density of the scattered wave packet for selected time instants and  $X_{apex}$  lateral tip displacements (0.0, 0.8, 1.6, and 2.0 nm). Size of the presentation window is 3.84 nm. Contour lines are drawn on square root scale. Each frame is normalized to its maximum density. Maximum density values are 4.2, 0.6, and  $0.07 \text{ nm}^{-2}$  for 1.7, 2.9, and 3.9 fs, respectively. Density in the tube region becomes appreciable on the lower right frame because of the renormalization.

The curve drawn by the tip apex point when the simulated tip is scanned over the nanotube while keeping the tunneling probability at a constant value is called a *quantum line cut* [14]. The good matching of the so defined quantum line cut (drawn by crosses in Fig. 8.) with the geometric line cut defined in Sec. 2.1. justifies the constant tip-sample separation ap-

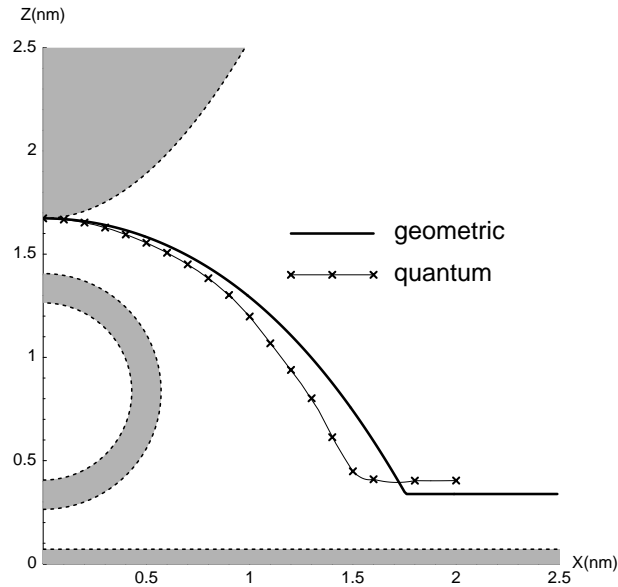


*Figure 8.* Comparison of geometric and quantum line cut. Thick solid line is the geometric line cut. Crosses show calculated points of the quantum line cut. A thin solid line connecting the crosses was drawn to guide the eye.

proximation. As seen in Fig. 8., however, the tip-sample separation is larger above the support plane than over the nanotube. This is because the WP has to tunnel through two tunnel resistances (tip-nanotube and nanotube-support) when the tip is above the nanotube but it has to tunnel through only one tunnel resistance when the tip is above the support plane. This causes a larger tunnel resistance above the nanotube than above the support plane which makes the feedback loop to retract the tip somewhat when the tunneling point is switched from the nanotube to the support plane. The different electronic structure of the nanotube and the support not included in this model causes a further increase of the tunnel gap above the support [14] as compared to that above the nanotube.

## 6. Summary and outlook

Scanning tunneling microscopy is an extremely attractive tool for imaging individual carbon nanostructures and to perform simultaneously spectroscopic measurements on the imaged nano-object. Because the imaging of supported 3D objects differs strongly from that of the flat, homogeneous surfaces, cautious image analysis and simulation are necessary to correctly interpret the experimental images.

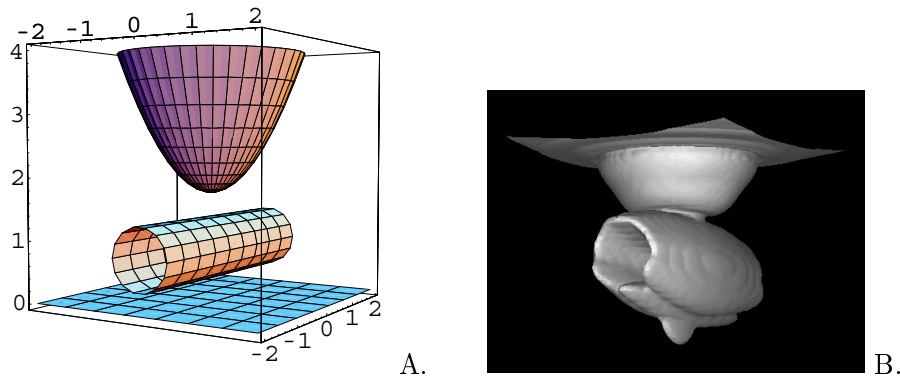


Figure 9. A) Geometric model of STM tip, nanotube and support surface. All dimensions are in  $nm$ . B) Snapshot (at  $t = 3.5 fs$ ) of the constant probability density surface of a wave packet tunneling through the tunnel junction shown in (A).

Recent developments in computer power and better algorithms also make it possible to use more realistic models in the simulations. These enhancements extend the sphere of the phenomena which can be interpreted by these simulations. As an example, in Fig. 9(b). shows a snapshot from the wave packet development calculated in three dimensions (3D) for the STM junction model of Fig. 9(a). Note that while the WP tunnels into the support surface (see the lower protrusion in the figure) it simultaneously spreads along the tube. Details are published elsewhere [18].

The tight-binding and wave packet dynamical STM simulation methods are simple enough to be utilized in the near future for more complex nanosystems like coiled nanotubes, Y-connections, nanotube crossings, etc.

### Acknowledgments

This work has been partly funded by the interuniversity research project on reduced dimensionality systems (PAI P4/10) of the Belgian Office for Scientific, Cultural, and Technical affairs, by the Hungarian OTKA Grant T 30435, and by EUS Centre of Excellence ICAI-CT-2000-70029. LPB gratefully acknowledges financial support from the Belgian FNRS.

### References

1. Kroto, H.W., Heath, J.R., O'Brien, S.C., Curl, R.F., and Smalley, R.E. (1985) C60: Buckminsterfullerene, *Nature* **318**, 162-163.
2. Scharff P. Fundamental Properties and Applications of Fullerene and Carbon Nanotube Systems, *This Volume*.
3. Dresselhaus, M. S., Dresselhaus, G., Eklund P. C. (1996) *Science of Fullerenes and Carbon Nanotubes*, Academic Press, San Diego.

4. Iijima, S. (1991) Helical microtubules of graphitic carbon, *Nature* **354**, 56-58.
5. Smith, B.W., Monthieux, M., and Luzzi, D.E. (1998) Encapsulated C60 in carbon nanotubes, *Nature* **396**, 323-324.
6. Ouyang, M., Huang, J.-L., Cheung, Ch.L., Lieber, Ch.M. (2001) Atomically resolved single-walled carbon nanotube intramolecular junctions, *Science* **291**, 97-100.
7. Nagy, P., Ehlich, R., Biró, L.P., Gyulai, J. (2000) Y-branching of single wall carbon nanotubes, *Appl. Phys. A* **70**, 481-483.
8. Binnig, G. and Rohrer, H. (1982) Scanning tunneling microscopy *Helv. Phys. Acta* **55**, 726-735.
9. Wiesendanger, R. (1994) *Scanning probe microscopy and spectroscopy*, Cambridge University Press, Cambridge.
10. Lucas, A.A., Morawitz, H., Henry, G.R., Vigneron, J.P., Lambin, Ph., Cutler, P.H., and Feuchtwang, T.W. (1988) Scattering theoretic approach to elastic one-electron tunneling through localized barriers: Applications to scanning tunneling microscopy, *Phys. Rev. B* **37**, 10708-10720.
11. Ge, M. and Sattler, K. (1994) STM of single-shell nanotubes of carbon, *Appl. Phys. Lett.* **65**, 2284-2286.
12. Venema, L.C., Meunier, V., Lambin, Ph., and Dekker, C. (2000) Atomic structure of carbon nanotubes from scanning tunneling microscopy, *Phys. Rev. B* **61**, 2991-2996.
13. Kim, Ph., Odom, T.W., Huang, J., and Lieber, C.M. (2000) STM study of single-walled carbon nanotubes, *Carbon* **38**, 1741-1744.
14. Márk, G.I., Biró, L.P., and Gyulai, J. (1998) Simulation of STM images of three-dimensional surfaces and comparison with experimental data: carbon nanotubes, *Phys. Rev. B* **58**, 12645-12648.
15. Clauss, W., Bergeron, D.J., Freitag, M., Kane, C.L., Mele, E.J., and Johnson, A.T. (1999) Electron backscattering on single-wall carbon nanotubes observed by STM, *Europhys. Lett.* **47**, 601-607.
16. Biró, L.P., Gyulai, J., Lambin, Ph., Nagy, J.B., Lazarescu, S., Márk, G.I., Fonseca, A., Surján, P.R., Szekeres, Zs., Thiry, P.A. Lucas, A.A. (1998) Scanning tunnelling microscopy (STM) imaging of carbon nanotubes, *Carbon* **36**, 689.
17. Márk, G.I., Biró, L.P., Gyulai, J., Thiry, P.A., Lucas, A.A., and Lambin, Ph. (2000) Simulation of scanning tunneling spectroscopy of supported carbon nanotubes, *Phys. Rev. B* **62**, 2797-2805.
18. Márk, G.I., Biró, L.P., Koós, A., Osváth, Z., Gyulai, J., Benito, A.M., Thiry, P.A., and Lambin, Ph. (in press) Charge spreading effects during 3D tunneling through a supported carbon nanotube, in *Electronic Properties of Novel Materials – Molecular Nanostructures*, March 2001, Kirchberg, Austria, AIP Conference Proceedings, edited by Kuzmany, H., Fink, J., Mehring, M., Roth, S.
19. Tersoff, J., Hamann, D.R. (1985) Theory of the scanning tunneling microscope, *Phys. Rev. B* **31**, 805-813.
20. Rubio, A., Sanchez-Portal, D., Artacho, E., Ordejon, P., and Soler, J.M. (1999) Electronic states in a finite carbon nanotube: A one-dimensional quantum box, *Phys. Rev. Lett.* **82**, 3520-3523; Rubio, A. (1999) Spectroscopic properties and STM images of carbon nanotubes, *Appl. Phys. A* **68**, 275-282.
21. Meunier, V. and Lambin, Ph. (1998) Tight-binding computation of the STM image of carbon nanotubes, *Phys. Rev. Lett.* **81**, 5888-5891.
22. Agrait, N., Rodrigo, J.G., and Vieira, S. (1992) On the transition from tunneling regime to point contact: graphite, *Ultramicroscopy* **42-44**, 177-183.
23. Charlier, J.C., Michenaud, J.P., and Lambin, Ph. (1992) Tight-binding density of electronic states of pregraphitic carbon, *Phys. Rev. B* **46**, 4540-4543.
24. Tománek, D. and Louie, S.G. (1988) First-principles calculations of highly asymmetric structure in scanning-tunneling-microscopy images of graphite, *Phys. Rev. B* **37**, 8327-8336.
25. Venema, L.C., Wildöer, J.W.G., Dekker, C., Rinzler, A.G., and Smalley, R.E. (1998) STM atomic resolution images of single-wall carbon nanotubes, *Appl. Phys. A* **66**,

- S153-S155.
26. Kane, C.L. and Mele, E.J. (1999) Broken symmetry in STM images of carbon nanotubes, *Phys. Rev. B* **59**, R12759-R12762.
  27. Wildöer, J.W.G., Venema, L.C., Rinzler, A.G., Smalley, R.E., and Dekker, C. (1998) Electronic structure of atomically resolved carbon nanotubes, *Nature* **391**, 59-62.
  28. Odom, T.W., Huang, J.L., Kim, Ph., and Lieber, Ch.M. (1998) Atomic structure and electronic properties of single-walled carbon nanotubes, *Nature* **391**, 62-64.
  29. Hassanien, A., Tokumoto, M., Kumazawa, Y., Kataura, H., Maniwa, Y., Suzuki, S., and Achiba, Y. (1998) Atomic structure and electronic properties of single-wall nanotubes probed by STM at room temperature, *Appl. Phys. Lett.* **73**, 3839-3841.